Shear Instability and Turbulent Mixing by Kuroshio Intrusion Into the Changjiang River Plume

Junbiao Tu[1] , **Jiaxue Wu[2]** , **Daidu Fan[1]** , **Zhiyu Liu[3]** , **Qianjiang Zhang[4]** , and **William Smyth[5]**

[1]State Key Laboratory of Marine Geology, Tongji University, Shanghai, China, [2]School of Marine Sciences, Sun Yat-sen University, Zhuhai, China, [3]State Key Laboratory of Marine Environmental Science, and Department of Physical Oceanography, College of Ocean and Earth Sciences, Xiamen University, Xiamen, China, [4]State Key Laboratory of Satellite Ocean Environment Dynamics, Second Institute of Oceanography, Ministry of Natural Resources, Hangzhou, China, [5]College of Oceanic and Atmospheric Sciences, Oregon State University, Corvallis, OR, USA

Abstract Shear instability is a dominant mechanism for mixing in the stratified oceans and coastal seas. For the first time, we present fine-scale, direct measurements of shear instabilities in the bottom front generated by the Kuroshio intrusion into the Changjiang (Yangtze) river plume. Shear instabilities were identified using a shipboard echo-sounder and the resulting turbulent mixing was quantified using a turbulence microstructure profiler. The shear instabilities generate vigorous turbulent mixing with dissipation rate and vertical diffusivity up to $O(10^{-4} \, \mathrm{m^2 \, s^{-3}})$ and $O(10^{-1} \, \mathrm{m^2 \, s^{-1}})$, respectively, comparable to values associated with shear instabilities observed in river plumes and western boundary currents but several orders of magnitude larger than typical values in the open ocean. The enhanced turbulence may contribute significantly to mixing between the Kuroshio water and coastal water and thereby alter the coastal biogeochemistry cycles.

Plain Language Summary Strong velocity shear across a density interface can produce instability, causing the interface to roll up to form a train of vortices ("billows") that subsequently break down into turbulence. This process is important in the vertical mixing of the oceanic interior and coastal seas. Using acoustic images, we find that this flow instability is induced by the interaction between the Kuroshio current and the Yangtze river plume. We also quantify the resulting turbulent mixing using high-resolution measurements. The turbulence efficiently mixes the Kuroshio and river plume-influence water and can change biogeochemistry cycles in the coastal seas.

1. Introduction

The Kelvin-Helmholtz (KH) shear instability is a major process converting energy from mean flow to small-scale turbulence in the stratified open ocean, coastal seas, and estuaries (Smyth & Moum, 2012). The structure and dynamics of shear instability as it grows to large amplitude and becomes turbulent have been widely studied in laboratory (e.g., Thorpe, 1973) and numerical (e.g., Kaminski & Smyth, 2019) experiments. At low Reynolds number (Re = UL/ν, where U, L, and ν are velocity scale, half-thickness of the shear layer, and kinematic viscosity, respectively), turbulent mixing occurs mainly at the core of the shear instabilities as a result of denser fluid rolling up to become gravitationally unstable (overturning) (e.g., Smyth et al., 2001). At high Re, mixing can occur on the braids connecting the cores due to secondary instabilities. The presence of secondary instabilities and their contribution to mixing has been hypothesized by Corcos and Sherman (1976), and further confirmed in high Re DNS studies (e.g., Van Dine et al. (2021), Re = 24,000), as well as field observations (Geyer et al., 2010), Re ~ 5×10^5; Chang et al. (2016), Re ~ 10^7). The flow stability in a stratified fluid is often assessed by the gradient Richardson number $Ri = N^2/S^2$, where $N^2 = (-g/\rho)(\partial\rho/\partial z)$ and $S^2 = (\partial u/\partial z)^2 + (\partial v/\partial z)^2$ are the buoyancy squared and the horizontal velocity shear squared, respectively. Miles (1961) and Howard (1961) showed instability is possible for Ri below a critical value of 0.25, indicating that the destabilizing effect of shear overcomes the stabilizing effect of stratification. However, Ri itself doesn't provide sufficient information to quantify turbulent mixing.

KH billows have been identified, mostly using echosounder images, in the stratified ocean and estuaries with strong shear (Chang et al., 2021; Moum et al., 2003, 2011; Smyth et al., 2011; van Haren et al., 2014; Van Haren & Gostiaux, 2010), in deep tidal channels (Seim & Gregg, 1994), in the Mediterranean Sea (Wesson & Gregg, 1994; Woods, 1968), in estuarine and plume flows stratified by salinity (Geyer et al., 2010; Geyer &

Farmer, 1989; Geyer & Smith, 1987; Holleman et al., 2016; Tedford et al., 2009) and suspended sediment (Tu et al., 2020, 2022), in a tidal intrusion front (Bassett et al., 2023; Geyer et al., 2024), and in the Kuroshio current interacting with rapidly changing topography (Chang et al., 2016; Hasegawa et al., 2021). In addition to assessing flow instability using Ri based on measured current and density profiles, recent observations were able to quantify the turbulent dissipation rates ε and vertical turbulent diffusivities K_ρ associated with shear instabilities (Chang et al., 2016, 2021; Geyer et al., 2010; Hasegawa et al., 2021; Tu et al., 2022). In highly stratified estuaries, Geyer et al. (2010) and Holleman et al. (2016) use ADVs (Acoustic Doppler velocimeters) and microconductivity probes to measure dissipations of TKE (turbulent kinetic energy) and salinity, both of which were elevated in the cores and braids of shear instabilities. In the Kuroshio Current, Chang et al. (2016) estimated dissipation rates using CTD profiling data based on the Thorpe scale method. Recently, microstructure shear probes were used to measure ε (Chang et al., 2021; Hasegawa et al., 2021). Combining with the buoyancy frequency N, vertical diffusivity was estimated based on the Thomas (1980) model ($K_\rho = \Gamma\varepsilon/N^2$, with $\Gamma = 0.2$ the flux coefficient). These observations reveal that shear instabilities create significant interfacial mixing in the strongly stratified flow (Arevalo et al., 2022; Kilcher & Nash, 2010; MacDonald & Geyer, 2004; Whitney et al., 2024).

The Kuroshio is a powerful western boundary current. Combined with the semidiurnal tide, the Kuroshio generates shear strong enough to overcome the density gradient with ambient waters. Therefore, shear instability occurs and greatly promotes turbulent mixing. A similar process has been found east of Taiwan (Chang et al., 2016) and southwest of Kyushu, Japan (Hasegawa et al., 2021). Hasegawa et al. (2021) found that shear instability enhanced turbulent mixing and caused strong vertical nitrate fluxes. It is well known that Kuroshio intrusion into the East China Sea modifies regional circulation and causes changes in salinity, temperature, and nutrients in the shelf seas (Yang et al., 2018).

The Changjiang (or Yangtze) River, one of the largest rivers in the world, inputs a large amount of freshwater to the estuary and its adjacent coastal sea. Three water masses mainly influence the estuary and adjacent seas: (a) the plume water, (b) the Subei coastal current from the north that is not seen from our observational data, and (c) a Kuroshio branch from the south (Beardsley et al., 1985; Chen et al., 1999; He et al., 2024). The Kuroshio branch can even intrude into the study area in the near-field of the Changjiang river plume (He et al., 2024; Zhang & Wu, 2018), creating a bottom salinity front and strong vertical stratification (Zhang & Wu, 2018). Using the same dataset as this study, Zhang and Wu (2018) comprehensively analyzed how the salinity intrusion modifies turbulence and suspended sediment dynamics in the benthic boundary layer.

Turbulent mixing associated with Kuroshio intrusion into the inner shelf of the East China Sea has rarely been studied (Wang et al., 2020). Wang et al. (2020) observed elevated ε (10^{-6} m^2 s^{-3}) derived from microstructure shear probes in the Kuroshio intrusion water compared to the overlying layer (10^{-8} m^2 s^{-3}). Our observations also include acoustic imagery that allows us to establish the mechanism of the turbulence, that is, shear instability and turbulence in the pycnocline induced by the bottom intrusion of the branch of Kuroshio current into a plume-influenced coastal sea.

2. Methodology

2.1. Data and Methods

The mooring observations were collected off the Changjiang River Estuary (Site A, Figure 1) during 22–23 September 2015, covering a 25 hr period. A bottom-mounted tripod was equipped with an upward-looking Acoustic Doppler current profiler (ADCP, 1,200 kHz, RDI), and an optical backscatter sensor (OBS) to measure turbidity, conductivity (accuracy ±0.07 mS/cm), and temperature (accuracy ±0.05°C). The ADCP recorded data at 1 Hz with a vertical cell size of 0.5 m and the lowest bin located 2.5 m above the bottom (mab). The OBS was deployed at 0.25 mab and a sampling frequency of 1 Hz. A dual-frequency echosounder (123/430 kHz) was mounted on the vessel side at 1 m below the sea surface to measure water depth and collect acoustic images, with a sampling rate of 3 Hz and a vertical resolution of 18 mm. Vertical profiles of shear, salinity, and temperature were measured using a tethered, free-falling MSS90 L (Sea & Sun Technology) microstructure profiler equipped with two shear probes, a fast-response thermistor, and a micro-conductivity sensor sampling at 1,024 Hz. Resolutions (accuracies) of the micro-conductivity and thermistor are 0.001 mS/cm (±0.02 mS/cm) and 0.0005°C (±0.01°C), respectively. The free-falling speed of the profiler is ~0.6 m s^{-1}, yielding a 20 m profile every ~30 s. Two ship-based downcast profiles were collected every ~20 min, yielding 146 profiles during the observational period.
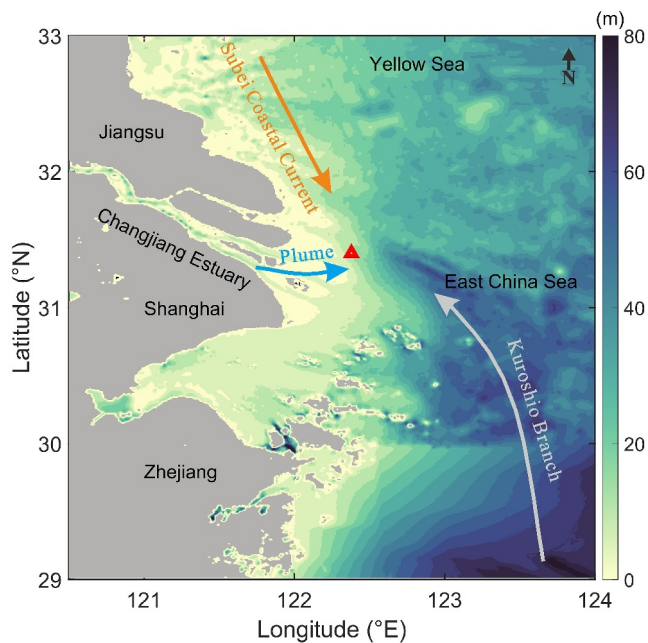
Figure 1. Bathymetry of the Changjiang River estuary and its adjacent sea. The mooring site is marked by a red triangle.

2.2. Turbulent Dissipation Estimates

Methods for estimating dissipation rates for TKE, salinity variance, and temperature variance are briefly introduced here (more details can be found in Supplementary Information S1). Assuming small-scale isotropy, the dissipation rate of turbulent kinetic energy (ε) and salinity (χ_S) were computed via $\varepsilon = 7.5\,\nu \int_{k_1}^{k2} \Phi_{u_z}(k)\,dk$ and $\chi_S = 6\,D_s \int_{k_a}^{k_b} \Phi_{S_z}(k)\,dk$, where ν and D_s are the molecular viscosity and salinity diffusivity of seawater. Φ_{u_z} and Φ_{S_z} are spectra of shear and salinity gradient, respectively. Φ_{S_z} was determined based on conductivity spectra and temperature spectra (Nash & Moum, 2002). The integrating range ($k_1 - k_2$ for ε and $k_a - k_b$ for χ_S) were determined using an iteration method until the observational and theoretical spectra converge (Nasmyth and Kraichnan spectral forms for ε and χ_S, respectively). We computed microstructure spectra based on half-overlapping 1 s segment data (1,024 data points) with Hamming windows. To ensure the quality of the dissipation estimates, we select a quality control criterion based on the mean absolute deviation (MAD) between the observed and theoretical spectra (Ruddick et al., 2000). Turbulent dissipations were interpolated onto a 0.5 m vertical grid. We estimated the dissipation rate of salinity variance assuming observed changes in density are determined by salinity. The dissipation rate of temperature variance (χ_T) was also calculated for comparison.

The Thomas (1980) model ($K_\rho = \Gamma \varepsilon / N^2$, assuming $\Gamma = 0.2$) has been widely used to infer turbulent diffusivity associated with shear instabilities (Chang et al., 2021; Hasegawa et al., 2021). However, a concern in the Osborn model is that Γ might not be a constant but decrease with increasing turbulent intensity (Monismith et al., 2018). Instead, we computed the vertical turbulent diffusivity using salinity/temperature dissipations and gradients based on the Thomas and Charles (1972) model ($K_T = \chi_T / (2T_z^2)$) which is based on the temperature variance equation. Unlike the Osborn model which relies on the TKE equation, this contains no gravitational term. Following Nash and Moum (2002) and Le Boyer et al. (2023), the vertical salinity diffusivity was estimated analogously as $K_S = \chi_S / (2S_z^2)$.

3. Results

3.1. Kuroshio Intrusion and Temporal Variations in Hydrography and Turbulence

The observed period covers two semidiurnal tidal cycles, with approximately identical flood and ebb durations (~6.5 hr, Figure 2). The mid-upper water column is dominated by the tidal current with northwestward flood current and southeastward ebb tidal currents (Figures 2c and 2d). Bottom dense water intrusion was observed at ~ Hour 6.5 (Figures 2a–2d); the salinity increases from 31.5 psu at Hour 6.5 to 33 psu at Hour 10; the temperature decreases from 24.5°C at Hour 6.5–24.1°C at Hour 10; the saline and cold water persists until the end of the observation (i.e., Hour 26), though a slight salinity decrease (0.2 psu) and temperature increase (0.1°C) were observed at the end of the second ebb (i.e., Hour 20). The bottom density front was also confirmed by the measurement of the near-bottom OBS-3A (Figure S2 in Supplementary Information S1). In line with Zhang and Wu (2018), we interpret the bottom front as a result of the Kuroshio branch intrusion.

An upper pycnocline (above ~15 mab) is formed due to the input of freshwater from the Changjiang River (Figure 1). However, as the measurements at these surface layers, especially the current and microstructure data, might be contaminated by the vessel, we chose to focus on the data at greater depths, that is, the lower pycnocline induced by Kuroshio branch intrusion. Following Inall et al. (2021), for each density profile, the upper (z_{upper}) and lower (z_{lower}) limits of the pycnocline were identified via $\rho(z_{upper}) = \rho_{max} - 0.7\,(\rho_{max} - \rho_{min})$, and $\rho(z_{lower}) = \rho_{min} + 0.7\,(\rho_{max} - \rho_{min})$, where ρ_{min} and ρ_{max} are the minimum and maximum densities in each profile excluding the surface 5 m. The boundaries of lower and upper pycnocline are indicated as black or white lines in Figure 2. The lower bound of the pycnocline rises after the salinity intrusion while the thickness of the pycnocline decreases, indicating a sharper density layer. The water column below z_{lower} roughly represents the benthic boundary layer whose thickness varied between ~2 and 9 m. The shelf water intrusion was also evident
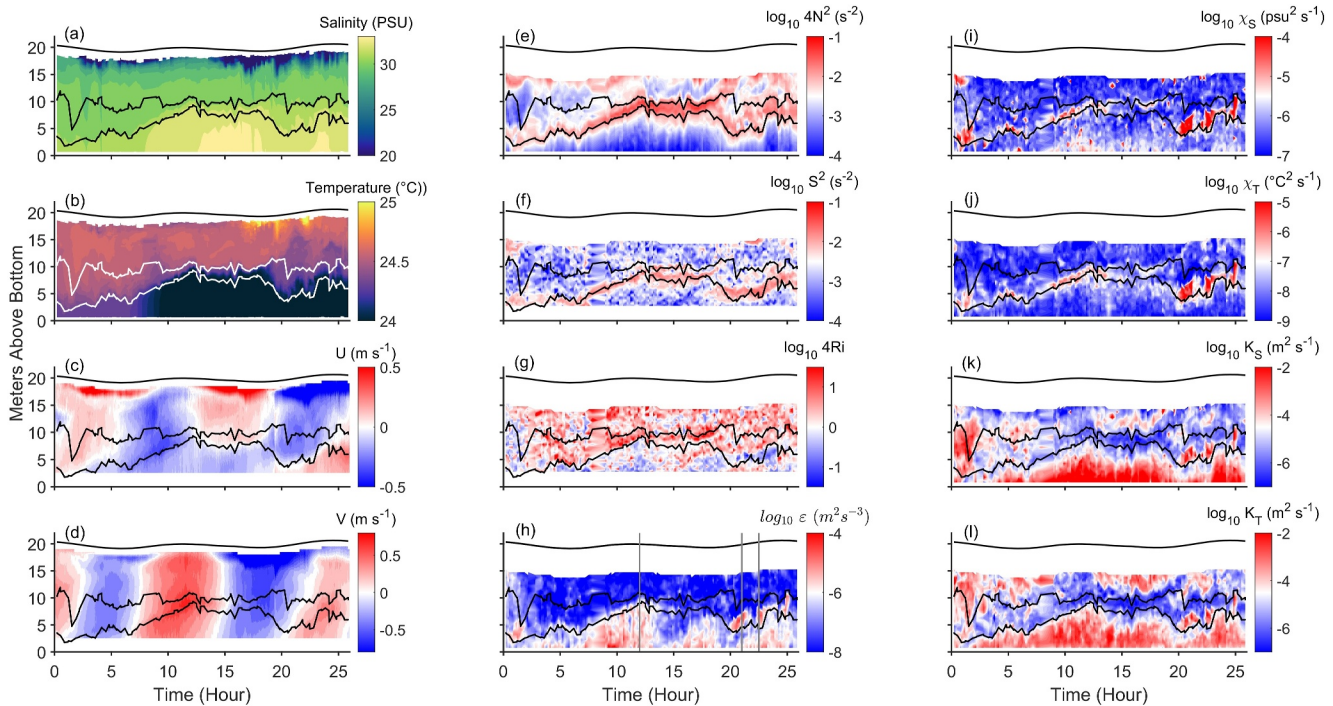
Figure 2. Depth-time variations in (a) salinity, (b) temperature, (c) zonal velocity, (d) meridional velocity, (e) four times buoyancy frequency squared, (f) horizontal velocity vertical shear squared, (g) gradient Richardson number, (h)TKE dissipation rate, the vertical gray lines indicate the selected times shown in Figure 3, (i) salinity variance dissipation rate (j) temperature variance dissipation rate (k) salinity based turbulent diffusivity, and (l) temperature based turbulent diffusivity. Black or white lines indicate the lower and upper boundaries of the pycnocline as defined in the text.

in the flow structure; both zonal and meridional flows in the lower water column (below ∼5 mab) are ∼1 hr ahead of those in the mid-upper water column.

The salinity intrusion creates intense stratification and shear at the lower bound of the pycnocline (Figures 2e and 2f). The depth-sorted stable density profile was used to estimate N^2 representative of background stratification. Maximum N^2 reached up to 0.015 s^{-2} (Hour 17.5 at 8.75 mab). Maximum S^2 is approximately 0.031 s^{-2} (Hour 16.5 at 8.25 mab). During Hour 7.5–18, the shear was not strong enough to overcome stratification, resulting in a relatively high Ri (>0.25) (Figure 2g). Below the pycnocline, Ri is mostly below 0.25, suggesting bottom boundary layer mixing. During Hour 19–25, shear intensified while stratification slightly weakened, resulting in low Ri around the lower bound of the pycnocline. A T-S diagram indicates that the upper layer represents plume waters, the intermediate layer is the plume-influenced layer, and the lower layer mainly consists of the Kuroshio intrusion waters (Figure S3 in Supplementary Information S1).

Large ε values (∼O (10^{-6}–10^{-5}) W/kg) were mostly observed in the bottom boundary layer (BBL), suggesting seabed-generated turbulence. During Hour 20–23, ε, χ_S, and χ_T peaked at the lower bound of the pycnocline. This suggests mechanisms other than the bottom turbulence cause the enhanced mixing. Given the intensified shear overcoming the stratification at the same region ($Ri < 0.25$), shear instability is a potential mechanism. Below the pycnocline χ_S and χ_T decreased significantly because the ambient salinity and temperature gradients were weaker; above the pycnocline χ_S and χ_T were also lower due to weaker turbulence and salinity/temperature gradients. Vertical diffusivities of salinity (K_S) and temperature (K_T) generally agree with each other, with decreased values observed within the pycnocline except for Hour 20–23 when shear instabilities were expected. In the BBL, diffusivities increased as the gradients in salinity/temperature decreased close to the bottom.

3.2. Stratification, Shear, and Instability

Echosounder images reveal wave-like structures suggestive of internal waves (Hour 12–19, Figure 3a) and KH billows (Hour 20–23, Figures 3b and 3c) within the pycnocline. Surface waves and bed forms were absent during the observational period. Three representative wavelike structures presented in 30 min-long echograms are
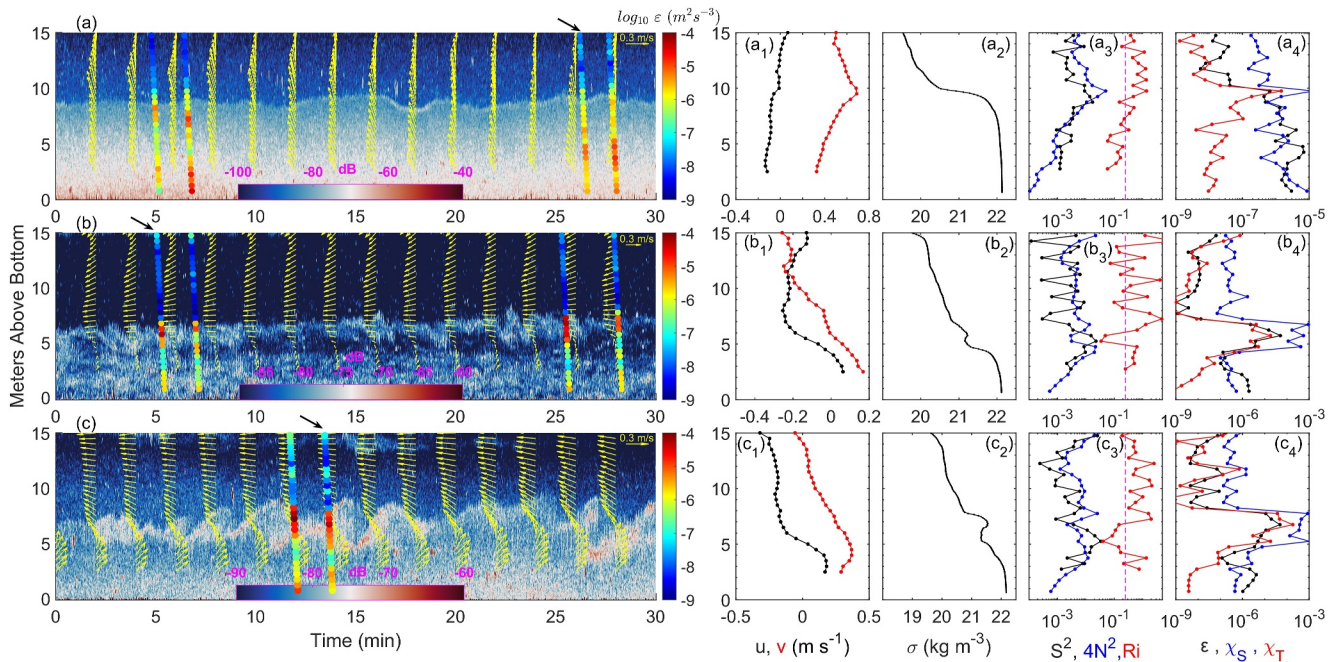
Figure 3. (a)–(c) Echosounder images superimposed with TKE dissipation rates (circles) and horizontal velocity (arrows, up for north), and selected individual profiles of zonal and meridional velocity, density anomaly ($\sigma = \rho - 1,000$), vertical shear squared (s^{-2}, black dotted line), four times buoyancy frequency squared (s^{-2}, blue dotted line), gradient Richardson number (red dotted line), dissipation rates of TKE (m^2 s^{-3}, black dotted line), salinity variance (psu^2 s^{-1}, blue dotted line), and temperature variance (°C^2 s^{-1}, red dotted line). The echosounder images presented in (a), (b), and (c) cover 30 min centered on Hours 12, 21, and 22.5, respectively. Black arrows indicate the profiles shown in the right panels (a1-c4). Note the red dashed lines in (a3-c3) represent $Ri = 1/4$.

described in what follows. As noted by Tu et al. (2022), an important caveat in the interpretation of the echogram is that the time dependence represents an unknown combination of advection by horizontal flow and true time evolution.

At Hour 12 (Figure 3a), the acoustic image shows clear signals of internal wavelike structure (Figure 3a). A sharp density interface around 9 mab induces strong stable stratification with N^2 reaching up to 0.013 s^{-2}. The corresponding shear ($S^2 = 0.018$ s^{-2}) is not strong enough to overcome stratification, yielding $Ri > 0.25$ at the density interface, likely favoring the formation of internal waves. Large TKE dissipation rates occur well below the density interface, and decrease dramatically above the pycnocline, suggesting that the density interface acts as a barrier for the BBL turbulence (colored dots in Figure 3a and ε profile in Figure 3a4). Both the dissipations of salinity and temperature (χ_S and χ_T) peaked at the interface due to large gradients in salinity and temperature.

At Hour 21 (Figure 3b), the acoustic signal was enhanced, suggesting the presence of Kelvin–Helmholtz (KH) wave-like billows and small-scale turbulence located at ~5–7 mab. Vertical shear was intensified at this acoustically enhanced layer (Figure 3b1); unstable stratification (density overturning) was localized in the layer 4.5–5.5 mab, possibly a result of shear instability (e.g., Chang et al. (2016)). N^2 (based on the sorted density profile) is less than S^2 below the billow center and greater above, resulting in Ri fluctuating around 0.25. The billows have asymmetric forms, especially those during Minute 2–8 and Minute 22–25, suggesting wave steepening and resembling the S-shape braids identified in estuaries and ocean interiors (e.g., Geyer et al., 2010; Tu et al., 2020). Dissipation rates of TKE, salinity, and temperature (ε, χ_S, and χ_T) are all elevated by ~2 decades compared to the fluid above and below. Therefore, we interpret these structures as Kelvin-Helmholtz billows.

Billows showing clear, symmetric braid-core structures were observed at Hour 22.5 at 4–9 mab (Figure 3c), well within the apparent shear layer (Figures 2f and 3c3). Note that the mean flow changed direction at the center of the billows, leading to strong vertical shear. Maximum S^2 was 0.03 s^{-2}, resulting in $Ri < 0.25$. Overturning was observed in the density profile. Again, turbulent dissipation values increased significantly at the billows' layers. Although the time dependence of the echogram (Figure 3c) represents an unknown combination of temporal and spatial variability, it is roughly consistent with the formation, growth, breaking, and decay of a train of K-H
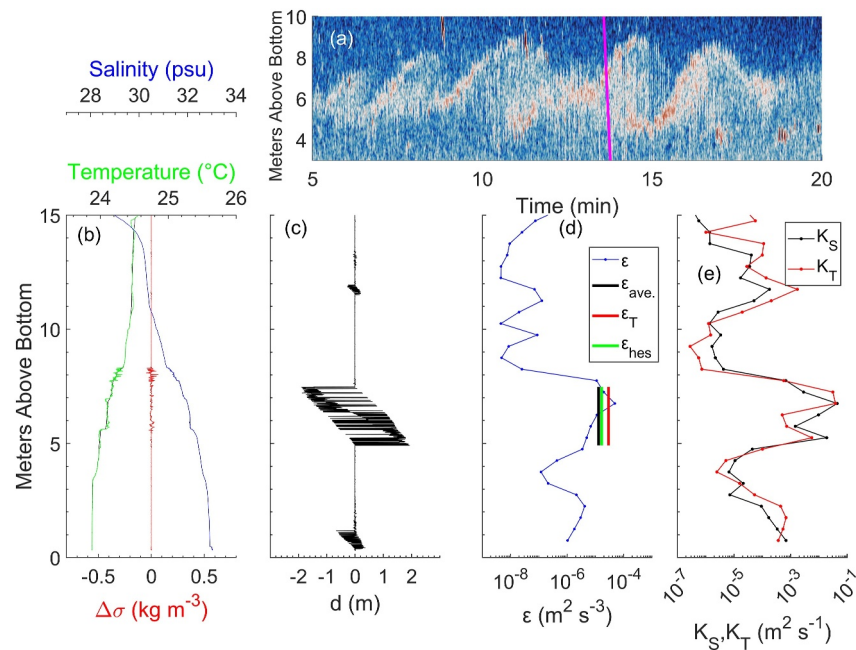
Figure 4. (a) An example of shear instabilities (Hour 22.5) revealed by echosounder backscatter, the magenta line indicates the time of the microstructure profile; (b) $\Delta\sigma$ (red), salinity (blue), temperature (green), depth-sorted profiles (black) profiles; (c) Thorpe displacements; (d) TKE dissipation rates based on shear probe data (blue curve), average within the overturning patch (black line), Thorpe scale (red line), and echosounder image using Tu et al. scaling; (e) turbulent vertical diffusivities of salinity (black line) and temperature (red line).

billows advected past an observer (e.g., Smyth et al., 2001; Tu et al., 2022). From 0 to 3 min, the acoustic signal was enhanced around 6 mab and wavelike features appeared. From 3 to 10 min the billows continued to grow. From 10 to 17 min, clear braid-core structures are identified, suggestive of classic KH billows. After 17 min the billows appear to break down into small-scale structure.

In summary, the three examples shown in Figure 3 suggest the presence of internal waves, shear instability, and small-scale structure. The internal waves are associated with a sharp density interface (thus strong stratification) and moderate shear, leading to $Ri > 0.25$, and weak mixing above the pycnocline. In cases identified as shear instability, intense shear, density overturning, $Ri < 0.25$, and elevated turbulent mixing are observed.

3.3. Overturning and Turbulence

Salinity and temperature profiles suggest that shear instability and turbulence cause density overturning. One example of CTD downcast associated with clear shear instabilities shown in the echosounder image is presented in Figure 4. The salinity profiles fluctuate strongly in billows' braid and core, consistent with those associated with shear instabilities observed in salt wedge estuary (Geyer et al., 2010) and Kuroshio current (Chang et al., 2016). Temperature inversions and fluctuations are also clear in the braid and core, as reported by (Chang et al., 2016). The S-shaped overturn was also identified using the difference between measured and sorted density $\Delta\sigma$. Secondary instability mediates the transition from instability to turbulence and billow collapse. Taking $U \sim 0.3 \,\mathrm{m\,s}^{-1}$, $L \sim 2$ m yields $\mathrm{Re} \sim 6 \times 10^5$, comparable to that in salt wedge estuary ($\mathrm{Re} \sim 5 \times 10^5$ (Geyer et al., 2010),). DNS studies suggest secondary instabilities are important in breaking down the primary billows into turbulent mixing in high Re flow (Van Dine et al., 2021), as confirmed by estuarine and oceanic observations (Geyer et al., 2010; van Haren et al., 2014). However, we are unable to recognize secondary billows, probably due to limited resolution, though overturning and enhanced turbulent mixing are observed in both the core and braid regions.

In stratified turbulence, the Ozmidov scale $L_O = \left(\varepsilon/N^3\right)^{1/2}$ represents the smallest scale influenced by buoyancy. Thus, TKE dissipation can be estimated via $\varepsilon_T = R_{OT}^2 N^3 L_T^2$ (Dillon, 1982; Thorpe, 1977), where $R_{OT} \sim 0.8$ is the ratio between the Ozmidov scale L_O and the Thorpe scale L_T. $L_T = \langle d^2 \rangle^{1/2}$ is the root-mean-square of the Thorpe

displacement (d) (Figure 4c). Thorpe displacement d is the depth difference of a water parcel between the original and sorted density profiles. It has been long debated that R_{OT} is not a constant but varies with the time evolution of the shear instability turbulence (Mater et al., 2015; Smyth et al., 2001). Another reason for the discrepancy between the measured and the Thorpe-scale-derived ε is the biases in identifying overturning events (Mater et al., 2015). For comparison with other observations of KH billows, we next estimate ε using the parameterization scheme proposed by Tu et al. (2022). They assume that the billow height (h_{es}) from the echosounder image is related to L_O via $h_{es}/L_O \sim C$ (a constant), and rearrange the definition of L_O to give $\varepsilon_{hes} = C^{-2}N^3h_{es}^2$, where N is averaged over L_T. By reconciling published observational datasets, they found $C \sim 12.5$. Given our observed maximum billow height of ∼5 m (Figure 4a), we obtain an ε estimate agreeing with the shear microstructure derived average over Figure 4d example turbulent patch ($\varepsilon_{ave.}/\varepsilon_{hes} \sim 0.8$, Figure 4d). The earlier microstructure profile shown in Figure 3c yields $\varepsilon_{ave.}/\varepsilon_{hes} \sim 0.9$, confirming the effectiveness of the Tu et al. (2022) scaling. While the Tu et al. (2022) scaling is useful, we must understand its caveat that the acoustic backscatter might not only reflect vertical density gradient, but could also be influenced by suspended particles, especially in coastal seas.

4. Discussion and Summary

The intrusion of the Kuroshio branch created a bottom salinity front and pycnocline which acted as a barrier to mixing between the intruding bottom saline water and the overlying fresher plume-influenced water. Interfacial waves occurred as a result of strong stratification with relatively weak shear ($Ri > 0.25$). As the shear intensified and overcame the stratification ($Ri < 0.25$), shear instabilities emerged. The shear instabilities drove density overturning and enhanced turbulence and mixing. The observed interfacial TKE dissipation rates (10^{-5}–10^{-4} m^2 s^{-3}) represent much more energetic turbulence compared to values observed within the oceanic thermocline (10^{-10}–10^{-6} m^2 s^{-3} (Gregg, 1989),). Corresponding values of turbulent diffusivity are on the orders of magnitude 10^{-2} m^2 s^{-1}, three orders greater than the common value found in the ocean interior (10^{-5} m^2 s^{-1}) (Ledwell et al., 1993), but consistent with observations associated with shear instabilities in a river plume and ocean interior (Chang et al., 2016; Geyer et al., 2010; Hasegawa et al., 2021; MacDonald & Geyer, 2004).

Shear instabilities are important in mixing the fresher coastal water and saline ocean water in stratified plumes and salt wedges, with pycnocline ε of O (10^{-4}–10^{-3}) m^2 s^{-3} and K_ρ of O (10^{-3}–10^{-2}) m^2 s^{-1} (Geyer et al., 2010; MacDonald & Geyer, 2004; McCabe et al., 2008; Orton & Jay, 2005). MacDonald and Geyer (2004) argued that the large values of ε relative to K_ρ are due to the large vertical stratification in the frontal zone. The interaction between Kuroshio and topography generates shear instability in the ocean interior (Chang et al., 2016), with ε reaching up to O (10^{-5}–10^{-4} m^2 s^{-3}) and K_ρ being O (10^{-2}–10^{-1} m^2 s^{-1}), respectively. Some 25 km offshore from our observational site, Wang et al. (2020) also observed the intrusion of Taiwan Warm Current (TWC, mainly consisting of Kuroshio subsurface water and Taiwan strait water) and enhanced turbulence with ε reaching up to 10^{-5} m^2 s^{-3} and vertical diffusivity ∼10^{-3} m^2 s^{-1}. In contrast to observations in highly stratified estuaries and river plumes (Geyer et al., 2010; MacDonald & Geyer, 2004), the Kuroshio observations are characterized by small values of ε relative to K_ρ as a result of the erosion of stratification due to intense shear instabilities. It is worth noting that K_ρ ($\Gamma\varepsilon/N^2$) might be overestimated in most studies as the assumption of constant mixing efficiency $\Gamma \sim 0.2$ could be violated under intense turbulence conditions (Caulfield, 2021; Monismith et al., 2018). In summary, shear instabilities were documented in coastal/plume regions (e.g., the Columbia River plume, Orton & Jay, 2005) and the mainstream of Kuroshio (e.g., Chang et al., 2016). Here, for the first time, we report shear instabilities induced by the intrusion of Kuroshio into a river plume-influenced region.

To understand the influence of shear instabilities on biogeochemical functioning, we must quantify mixing and understand the physical processes leading to turbulence. Is the observed turbulence sufficient to significantly mix the Kuroshio and Changjiang plume-influenced waters? Suppose that a turbulent layer of thickness Δz is mixed over a time scale Δt. This requires turbulent diffusivity of order $\Delta z^2/\Delta t$. With an independent estimate of the saline diffusivity K_S (as shown in Figure 4e), we can rearrange this relation to estimate the mixing time scale $\Delta t \sim \Delta z^2/K_s$. In the present case, the diffusivity is ∼10^{-2} m^2/s and the thickness of the layer is ∼5 m, so that our time scale for mixing is ∼1 hr. Though crude, this estimate suggests a significant change to the water column hydrography over the tidal cycle.

Enhanced mixing can cause ecologically important exchanges of nutrients between the bottom layer Kuroshio waters and the river plume-influenced waters because nutrient compositions in the plume and Kuroshio branch

waters differ significantly. Particularly, the onshore intrusion of Kuroshio is crucial for supplying phosphate (Zhou et al., 2019), which is further transported upward through upwelling (Yang et al., 2013). The Kuroshio intrusion into the East China Sea is present all year round, though the intrusion path varies seasonally (He et al., 2024; Wang et al., 2019; Yang et al., 2018). This indicates that the Kuroshio Current can be more energetic elsewhere across the East China Sea, where the intrusion is more intense, and shear instability might play a more important role in mixing the ocean and coastal/plume waters.

Data Availability Statement

The data are publicly available at Zenodo (Tu, 2024).

References

Arevalo, F. M., Álvarez-Silva, Ó., Caceres-Euse, A., & Cardona, Y. (2022). Mixing mechanisms at the strongly-stratified Magdalena River's estuary and plume. *Estuarine, Coastal and Shelf Science*, *277*, 108077. https://doi.org/10.1016/j.ecss.2022.108077

Bassett, C., Lavery, A. C., Ralston, D., Geyer, W. R., Jurisa, J. T., Thomson, J., et al. (2023). Acoustic backscattering at a tidal intrusion front. *Progress in Oceanography*, *219*, 103167. https://doi.org/10.1016/j.pocean.2023.103167

Beardsley, R., Limeburner, R., Yu, H., & Cannon, G. (1985). Discharge of the Changjiang (Yangtze river) into the East China sea. *Continental Shelf Research*, *4*(1–2), 57–76. https://doi.org/10.1016/0278-4343(85)90022-6

Caulfield, C. (2021). Layering, instabilities, and mixing in turbulent stratified flows. *Annual Review of Fluid Mechanics*, *53*(1), 113–145. https://doi.org/10.1146/annurev-fluid-042320-100458

Chang, M.-H., Cheng, Y.-H., Yang, Y. J., Jan, S., Ramp, S. R., Reeder, D. B., et al. (2021). Direct measurements reveal instabilities and turbulence within large amplitude internal solitary waves beneath the ocean. *Communications Earth & Environment*, *2*(1), 15. https://doi.org/10.1038/s43247-020-00083-6

Chang, M. H., Jheng, S. Y., & Lien, R. C. (2016). Trains of large Kelvin-Helmholtz billows observed in the Kuroshio above a seamount. *Geophysical Research Letters*, *43*(16), 8654–8661. https://doi.org/10.1002/2016gl069462

Chen, J., Li, D., Chen, B., Hu, F., Zhu, H., & Liu, C. (1999). The processes of dynamic sedimentation in the Changjiang Estuary. *Journal of Sea Research*, *41*(1–2), 129–140. https://doi.org/10.1016/s1385-1101(98)00047-1

Corcos, G. M., & Sherman, F. S. (1976). Vorticity concentration and the dynamics of unstable free shear layers. *Journal of Fluid Mechanics*, *73*(2), 241–264. https://doi.org/10.1017/s0022112076001365

Dillon, T. M. (1982). Vertical overturns: A comparison of Thorpe and Ozmidov length scales. *Journal of Geophysical Research*, *87*(C12), 9601–9613. https://doi.org/10.1029/JC087iC12p09601

Geyer, W. R., & Farmer, D. M. (1989). Tide-induced variation of the dynamics of a salt wedge estuary. *Journal of Physical Oceanography*, *19*(8), 1060–1072. https://doi.org/10.1175/1520-0485(1989)019<1060:tivotd>2.0.co;2

Geyer, W. R., Lavery, A. C., Scully, M. E., & Trowbridge, J. H. (2010). Mixing by shear instability at high Reynolds number. *Geophysical Research Letters*, *37*(22). https://doi.org/10.1029/2010gl045272

Geyer, W. R., Ralston, D. K., Haller, M. C., Bassett, C., & Honegger, D. (2024). The structure and dynamics of an estuarine tidal intrusion front. *Journal of Geophysical Research: Oceans*, *129*(2), e2023JC020371. https://doi.org/10.1029/2023JC020371

Geyer, W. R., & Smith, J. D. (1987). Shear instability in a highly stratified estuary. *Journal of Physical Oceanography*, *17*(10), 1668–1679. https://doi.org/10.1175/1520-0485(1987)017<1668:siiahs>2.0.co;2

Gregg, M. C. (1989). Scaling turbulent dissipation in the thermocline. *Journal of Geophysical Research*, *94*(C7), 9686–9698. https://doi.org/10.1029/jc094ic07p09686

Hasegawa, D., Matsuno, T., Tsutsumi, E., Senjyu, T., Endoh, T., Tanaka, T., et al. (2021). How a small reef in the Kuroshio cultivates the ocean. *Geophysical Research Letters*, *48*(7), e2020GL092063. https://doi.org/10.1029/2020gl092063

He, Z., Yang, D., Yin, B., & Wu, H. (2024). Two key mechanisms of large-scale cross-shelf penetrating fronts in the East China Sea: Flow convergence and thermocline undulation. *Journal of Geophysical Research: Oceans*, *129*(2), e2022JC019075. https://doi.org/10.1029/2022jc019075

Holleman, R., Geyer, W., & Ralston, D. (2016). Stratified turbulence and mixing efficiency in a salt wedge estuary. *Journal of Physical Oceanography*, *46*(6), 1769–1783. https://doi.org/10.1175/jpo-d-15-0193.1

Howard, L. N. (1961). Note on a paper of John W. Miles. *Journal of Fluid Mechanics*, *10*(04), 509–512. https://doi.org/10.1017/s0022112061000317

Inall, M. E., Toberman, M., Polton, J. A., Palmer, M. R., Green, J. A. M., & Rippeth, T. P. (2021). Shelf seas baroclinic energy loss: Pycnocline mixing and bottom boundary layer dissipation. *Journal of Geophysical Research: Oceans*, *126*(8), e2020JC016528. https://doi.org/10.1029/2020JC016528

Kaminski, A., & Smyth, W. (2019). Stratified shear instability in a field of pre-existing turbulence. *Journal of Fluid Mechanics*, *862*, 639–658. https://doi.org/10.1017/jfm.2018.973

Kilcher, L. F., & Nash, J. D. (2010). Structure and dynamics of the Columbia River tidal plume front. *Journal of Geophysical Research*, *115*(C5). https://doi.org/10.1029/2009jc006066

Le Boyer, A., Couto, N., Alford, M. H., Drake, H. F., Bluteau, C. E., Hughes, K. G., et al. (2023). Turbulent diapycnal fluxes as a pilot essential ocean variable. *Frontiers in Marine Science*, *10*, 1241023. https://doi.org/10.3389/fmars.2023.1241023

Ledwell, J. R., Watson, A. J., & Law, C. S. (1993). Evidence for slow mixing across the pycnocline from an open-ocean tracer-release experiment. *Nature*, *364*(6439), 701–703. https://doi.org/10.1038/364701a0

MacDonald, D. G., & Geyer, W. R. (2004). Turbulent energy production and entrainment at a highly stratified estuarine front. *Journal of Geophysical Research*, *109*(C5). https://doi.org/10.1029/2003jc002094

Mater, B. D., Venayagamoorthy, S. K., Laurent, L. S., & Moum, J. N. (2015). Biases in Thorpe-scale estimates of turbulence dissipation. Part I: Assessments from large-scale overturns in oceanographic data. *Journal of Physical Oceanography*, *45*(10), 2497–2521. https://doi.org/10.1175/jpo-d-14-0128.1

McCabe, R. M., Hickey, B. M., & MacCready, P. (2008). Observational estimates of entrainment and vertical salt flux in the interior of a spreading river plume. *Journal of Geophysical Research*, *113*(C8). https://doi.org/10.1029/2007jc004361

Miles, J. W. (1961). On the stability of heterogeneous shear flows. *Journal of Fluid Mechanics*, *10*(04), 496–508. https://doi.org/10.1017/s0022112061000305

Monismith, S. G., Koseff, J. R., & White, B. L. (2018). Mixing efficiency in the presence of stratification: When is it constant? *Geophysical Research Letters*, *45*(11), 5627–5634. https://doi.org/10.1029/2018gl077229

Moum, J., Farmer, D., Smyth, W., Armi, L., & Vagle, S. (2003). Structure and generation of turbulence at interfaces strained by internal solitary waves propagating shoreward over the continental shelf. *Journal of Physical Oceanography*, *33*(10), 2093–2112. https://doi.org/10.1175/1520-0485(2003)033<2093:sagota>2.0.co;2

Moum, J., Nash, J., & Smyth, W. (2011). Narrowband oscillations in the upper equatorial ocean. Part I: Interpretation as shear instabilities. *Journal of Physical Oceanography*, *41*(3), 397–411. https://doi.org/10.1175/2010jpo4450.1

Nash, J. D., & Moum, J. N. (2002). Microstructure estimates of turbulent salinity flux and the dissipation spectrum of salinity. *Journal of Physical Oceanography*, *32*(8), 2312–2333. https://doi.org/10.1175/1520-0485(2002)032<2312:meotsf>2.0.co;2

Orton, P. M., & Jay, D. A. (2005). Observations at the tidal plume front of a high-volume river outflow. *Geophysical Research Letters*, *32*(11). https://doi.org/10.1029/2005gl022372

Ruddick, B., Anis, A., & Thompson, K. (2000). Maximum likelihood spectral fitting: The Batchelor spectrum. *Journal of Atmospheric and Oceanic Technology*, *17*(11), 1541–1555. https://doi.org/10.1175/1520-0426(2000)017<1541:mlsftb>2.0.co;2

Seim, H. E., & Gregg, M. C. (1994). Detailed observations of a naturally occurring shear instability. *Journal of Geophysical Research*, *99*(C5), 10049–10073. https://doi.org/10.1029/94jc00168

Smyth, W., Moum, J., & Caldwell, D. (2001). The efficiency of mixing in turbulent patches: Inferences from direct simulations and microstructure observations. *Journal of Physical Oceanography*, *31*(8), 1969–1992. https://doi.org/10.1175/1520-0485(2001)031<1969:teomit>2.0.co;2

Smyth, W., Moum, J., & Nash, J. (2011). Narrowband oscillations in the upper equatorial ocean. Part II: Properties of shear instabilities. *Journal of Physical Oceanography*, *41*(3), 412–428. https://doi.org/10.1175/2010jpo4451.1

Smyth, W. D., & Moum, J. N. (2012). Ocean mixing by Kelvin-Helmholtz instability. *Oceanography*, *25*(2), 140–149. https://doi.org/10.5670/oceanog.2012.49

Tedford, E., Carpenter, J., Pawlowicz, R., Pieters, R., & Lawrence, G. A. (2009). Observation and analysis of shear instability in the Fraser River estuary. *Journal of Geophysical Research*, *114*(C11). https://doi.org/10.1029/2009jc005313

Thomas, R. O. (1980). Estimates of the local rate of vertical diffusion from dissipation measurements. *Journal of Physical Oceanography*, *10*(1), 83–89. https://doi.org/10.1175/1520-0485(1980)010<0083:eotlro>2.0.co;2

Thomas, R. O., & Charles, S. C. (1972). Oceanic fine structure. *Geophysical Fluid Dynamics*, *3*(4), 321–345. https://doi.org/10.1080/03091927208236085

Thorpe, S. (1973). Experiments on instability and turbulence in a stratified shear flow. *Journal of Fluid Mechanics*, *61*(4), 731–751. https://doi.org/10.1017/s0022112073000911

Thorpe, S. A. (1977). Turbulence and mixing in a Scottish loch. *Philosophical Transactions of the Royal Society of London - Series A: Mathematical and Physical Sciences*, *286*(1334), 125–181.

Tu, J. (2024). data for submission to GRL by Tu et al. *Zenodo*. [Dataset]. https://doi.org/10.5281/zenodo.11312846

Tu, J., Fan, D., Lian, Q., Liu, Z., Liu, W., Kaminski, A., & Smyth, W. (2020). Acoustic observations of Kelvin-Helmholtz billows on an estuarine lutocline. *Journal of Geophysical Research: Oceans*, *125*(4), e2019JC015383. https://doi.org/10.1029/2019jc015383

Tu, J., Fan, D., Sun, F., Kaminski, A., & Smyth, W. (2022). Shear instabilities and stratified turbulence in an estuarine fluid mud. *Journal of Physical Oceanography*, *52*(9), 2257–2271. https://doi.org/10.1175/jpo-d-21-0230.1

Van Dine, A., Pham, H. T., & Sarkar, S. (2021). Turbulent shear layers in a uniformly stratified background: DNS at high Reynolds number. *Journal of Fluid Mechanics*, *916*, A42. https://doi.org/10.1017/jfm.2021.212

Van Haren, H., & Gostiaux, L. (2010). A deep-ocean Kelvin-Helmholtz billow train. *Geophysical Research Letters*, *37*(3). https://doi.org/10.1029/2009gl041890

van Haren, H., Gostiaux, L., Morozov, E., & Tarakanov, R. (2014). Extremely long Kelvin-Kelmholtz billow trains in the romanche fracture zone. *Geophysical Research Letters*, *41*(23), 8445–8451. https://doi.org/10.1002/2014gl062421

Wang, J., Yu, F., Ren, Q., Si, G., & Wei, C. (2019). The observed variations of the north intrusion of the bottom Taiwan Warm Current Inshore Branch and its response to wind. *Regional Studies in Marine Science*, *30*, 100690. https://doi.org/10.1016/j.rsma.2019.100690

Wang, J., Yu, F., Ren, Q., & Wei, C. (2020). Spatial and temporal variability of turbulent mixing in the near-field of the Changjiang River. *Journal of Oceanology and Limnology*, *38*(4), 1138–1152. https://doi.org/10.1007/s00343-020-0008-7

Wesson, J., & Gregg, M. (1994). Mixing at camarinal sill in the strait of Gibraltar. *Journal of Geophysical Research*, *99*(C5), 9847–9878. https://doi.org/10.1029/94jc00256

Whitney, M. M., Spicer, P., MacDonald, D. G., Huguenard, K. D., Cole, K. L., Jia, Y., & Delatolas, N. (2024). Mixing of the Connecticut River plume during ambient flood tides: Spatial heterogeneity and contributions of bottom-generated and interfacial mixing. *Journal of Geophysical Research: Oceans*, *129*(3), e2023JC020423. https://doi.org/10.1029/2023jc020423

Woods, J. (1968). Wave-induced shear instability in the summer thermocline. *Journal of Fluid Mechanics*, *32*(4), 791–800. https://doi.org/10.1017/s0022112068001035

Yang, D., Yin, B., Chai, F., Feng, X., Xue, H., Gao, G., & Yu, F. (2018). The onshore intrusion of Kuroshio subsurface water from February to July and a mechanism for the intrusion variation. *Progress in Oceanography*, *167*, 97–115. https://doi.org/10.1016/j.pocean.2018.08.004

Yang, D., Yin, B., Sun, J., & Zhang, Y. (2013). Numerical study on the origins and the forcing mechanism of the phosphate in upwelling areas off the coast of Zhejiang province, China in summer. *Journal of Marine Systems*, *123*, 1–18. https://doi.org/10.1016/j.jmarsys.2013.04.002

Zhang, Q., & Wu, J. (2018). Sediment suspension by straining-induced convection at the head of salinity intrusion. *Journal of Geophysical Research: Oceans*, *123*(1), 656–671. https://doi.org/10.1002/2017jc013192

Zhou, Z. X., Yu, R. C., Sun, C., Feng, M., & Zhou, M. J. (2019). Impacts of Changjiang River discharge and Kuroshio intrusion on the diatom and dinoflagellate blooms in the East China sea. *Journal of Geophysical Research: Oceans*, *124*(7), 5244–5257. https://doi.org/10.1029/2019jc015158

References From the Supporting Information

Fer, I., Baumann, T. M., Koenig, Z., Muilwijk, M., & Tippenhauer, S. (2022). Upper-Ocean turbulence structure and ocean-ice drag coefficient estimates using an ascending microstructure profiler during the MOSAiC drift. *Journal of Geophysical Research: Oceans*, *127*(9), e2022JC018751. https://doi.org/10.1029/2022jc018751

Goodman, L., Levine, E. R., & Lueck, R. G. (2006). On measuring the terms of the turbulent kinetic energy budget from an AUV. *Journal of Atmospheric and Oceanic Technology*, *23*(7), 977–990. https://doi.org/10.1175/jtech1889.1

Kraichnan, R. H. (1968). Small-scale structure of a scalar field convected by turbulence. *The Physics of Fluids*, *11*(5), 945–953. https://doi.org/10.1063/1.1692063

Merrifield, S. T., Laurent, L. S., Owens, B., Thurnherr, A. M., & Toole, J. M. (2016). Enhanced diapycnal diffusivity in intrusive regions of the Drake Passage. *Journal of Physical Oceanography*, *46*(4), 1309–1321. https://doi.org/10.1175/jpo-d-15-0068.1

Moum, J., Gregg, M., Lien, R., & Carr, M. (1995). Comparison of turbulence kinetic energy dissipation rate estimates from two ocean microstructure profilers. *Journal of Atmospheric and Oceanic Technology*, *12*(2), 346–366. https://doi.org/10.1175/1520-0426(1995)012<0346:cotked>2.0.co;2

Moum, J. N., Rudnick, D. L., Shroyer, E. L., Hughes, K. G., Reineman, B. D., Grindley, K., et al. (2023). Flippin'χ SOLO, an upper-ocean autonomous turbulence-profiling float. *Journal of Atmospheric and Oceanic Technology*, *40*(5), 629–644. https://doi.org/10.1175/jtech-d-22-0067.1

Welch, P. D. (1967). The use of fast fourier transform for the estimation of power spectra: A method based on time averaging over short, modified periodograms. *IEEE Transactions on Audio and Electroacoustics*, *15*(2), 70–73. AU-15. https://doi.org/10.1109/tau.1967.1161901